



A hybrid compass mechanism combining radical pairs and magnetite crystals

P. J. Hore^{a,1}

Edited by Steven Boxer, Stanford University, Stanford, CA; received August 29, 2025; accepted January 26, 2026

That night-migratory songbirds have a magnetic compass sense is undisputed. The nature of the sensor, however, is far from certain. The two leading hypotheses are organic radical pairs in cryptochrome flavoproteins and crystals of inorganic magnetic minerals such as magnetite. Here, we propose a magnetoreception mechanism that combines radical pair chemistry with magnetite nanoparticles. Instead of directly detecting the tiny dependence of a radical pair reaction on the direction of the Earth's (~50 μT) magnetic field, this hybrid sensor uses a magnetic particle to amplify the Earth's field. Directional information is thereby encoded in the response of nearby radical pairs to the intensity of a much stronger (~5 mT) magnetic field. The result is a magnetoreceptor with potentially 10 to 100-fold greater sensitivity than afforded by radical pairs alone.

magnetoreception | radical pair mechanism | magnetic compass sense | magnetite

Every year billions of small songbirds fly spectacular distances between their breeding and wintering grounds, navigating with the help of an internal, light-dependent, magnetic inclination compass (1, 2). Sixty years after the discovery of this remarkable sense, the identity of the sensor and the biophysics of its action are still obscure (3, 4). Two hypotheses stand out: radical pairs and magnetic particles. The former proposes that photochemical reactions encode the direction of the Earth's magnetic field (25 to 65 μT) via the coherent spin dynamics of cryptochrome photoreceptors (5, 6). The latter suggests that intracellular crystals of biogenic iron-containing minerals, e.g., magnetite (Fe_3O_4), rotate into alignment with the Earth's field thereby opening mechanosensitive transmembrane ion channels (7, 8).

The magnetite hypothesis has solid theoretical foundations but no receptor has yet been identified, either for the map sense or the compass sense in any animal (3, 4, 7). The cryptochrome hypothesis is based on an established mechanism for the magnetic sensitivity of organic radical reactions (9). The photoreceptor protein cryptochrome 4a (CRY4a) (10–16), located in double-cone photoreceptor cells in the birds' retinas (17), is thought to be the magnetoreceptor although much of the supporting evidence is indirect (3, 4, 18). Radical pairs formed photochemically in purified avian CRY4a are magnetically sensitive, and meet the requirements for a light-dependent sensor indifferent to the polarity of the external magnetic field (14, 19, 20). However, there are major questions about whether the *in vivo* response of any radical pair reaction to a magnetic field 10 to 100 times weaker than a small refrigerator magnet could be sufficient to form the basis of a viable geomagnetic sensor (21).

The low sensitivity of radical pairs to submillitesla magnetic fields can, in part, be traced back to the internal magnetic (hyperfine) interactions between electron and nuclear spins. In CRY4a, the ^1H and ^{14}N hyperfine tensors that have the largest anisotropy do not, for the most part, have mutually aligned principal axes, causing the magnetic anisotropy of the spin system as a whole to be substantially lower than that of the individual hyperfine interactions. In addition, the nuclei that have more nearly isotropic hyperfine tensors provide little directional information and tend to dilute that available from their more anisotropic neighbors. Matters are not helped by the dipolar coupling of the two electron spins (22), by spin relaxation (23, 24), by suboptimal reaction kinetics (6), or by imperfect protein alignment (25), all of which can further attenuate the magnetic response. It is unsurprising therefore that as spin dynamics simulations of radical pair magnetoreceptors are made progressively more realistic, e.g. by including more nuclear spins, so the predicted magnetic field effects become ever smaller (21, 26).

We propose here a hybrid magnetic compass mechanism that combines elements of the cryptochrome and magnetite hypotheses in a way that could afford substantially greater sensitivity than normally expected from the "standard" radical pair model, as originally described by Ritz et al. (5). The concept is distinct from earlier experimental work (27–32) and theoretical treatments (8, 33–39) of radical pairs in the neighborhood of magnetic nanostructures. Those studies focused on heterogeneous catalysis of intersystem crossing

Significance

Small night-migratory songbirds navigate thousands of kilometers assisted by an internal magnetic compass whose underlying biophysical mechanism is largely obscure. Evidence suggests that light-sensitive molecules in the birds' eyes can respond to the Earth's magnetic field although it is far from clear that the ensuing signal is strong enough for reliable navigation. We propose a variant of this hypothesis in which these magnetically sensitive molecules operate alongside magnetic iron oxide particles which amplify the Earth's field. The model predicts that this partnership could increase the directional response of the sensor by up to 100-fold. By bridging biology and physics, this framework advances understanding of how migratory birds accomplish one of Nature's most extraordinary navigational feats.

Author affiliations: ^aDepartment of Chemistry, University of Oxford, Oxford OX1 3QZ, United Kingdom

Author contributions: P.J.H. designed research; performed research; analyzed data; and wrote the paper.

The author declares no competing interest.

This article is a PNAS Direct Submission.

Copyright © 2026 the Author(s). Published by PNAS. This open access article is distributed under Creative Commons Attribution License 4.0 (CC BY).

¹Email: peter.hore@chem.ox.ac.uk.

This article contains supporting information online at <https://www.pnas.org/lookup/suppl/doi:10.1073/pnas.2524093123/-DCSupplemental>.

Published February 19, 2026.

(33), magneto-fluorescence imaging (30), magnetic-field mapping (31), transduction of time-dependent magnetic fields (37, 39), and in vivo tests for a radical-pair direction sensor (38). The present proposal also differs from previous discussions of hybrid magnetic compass mechanisms which rely on either the strong magnetic-field gradient close to the surface of a nanoparticle (33, 34), the microtesla magnetic field further away from a much larger magnet (35), or the delicate balance between elastic and magnetic torques on a nanomagnet whose free rotation is hindered by cytoskeletal attachment (8, 36). Nor is it directly connected to the MagR hypothesis (40) in which CRY4 is proposed to interact with a protein whose magnetic properties appear to originate in a small number of weakly coupled iron atoms.

Results

Standard Radical Pair Mechanism. Avian CRY4a is a ~64 kDa flavoprotein containing a noncovalently bound FAD (flavin adenine dinucleotide) chromophore. Blue-light irradiation excites the FAD, triggering the formation of a spin-singlet $\text{FAD}^{\bullet-} \text{TrpH}^{\bullet+}$ radical pair via consecutive electron transfers along a chain of four tryptophan (TrpH) residues to the excited FAD (10–16, 19, 20). This singlet state coherently interconverts with the spin-triplet radical pair and both are transformed into a signaling state of the protein with a quantum yield that encodes the intensity and the direction of an external magnetic field via its influence on the singlet-triplet spin dynamics (5, 6). Although $\text{FAD}^{\bullet-} \text{TrpH}^{\bullet+}$ accounts for the magnetic field effects observed for purified avian CRY4a (14, 20), it is conceivable that a different FAD-containing radical pair, formed during the dark reoxidation of the photoreduced protein, could be magnetically sensitive in vivo (41, 42). Given the uncertain identity and properties of this state, we focus here on $\text{FAD}^{\bullet-} \text{TrpH}^{\bullet+}$, although our proposed mechanism is also applicable to these “dark” radical pairs provided their spin relaxation is not too fast (43).

To illustrate the sensitivity issue with the standard model and its dependence on the number of nuclear spins (n_{nuc}) coupled to the two electrons, Fig. 1 shows calculated magnetic field effects on toy models of $\text{FAD}^{\bullet-} \text{TrpH}^{\bullet+}$. Details of these calculations are given in the SI Appendix, section S1. Starting with the two nuclei in $\text{FAD}^{\bullet-}$ that have the largest hyperfine anisotropy (Fig. 1A), nuclei were added one at a time to the $\text{TrpH}^{\bullet+}$ radical (Fig. 1B–D). The four panels show the ranges (shaded areas) and averages (solid lines) of the yield of the product formed from the triplet radical pair (Φ_{T}), calculated for 400 hemispherically distributed directions of a magnetic field with strength in the range $B = 0.05\text{--}50$ mT. In the following, we refer to the maximum-minus-minimum $\Phi_{\text{T}}(B)$ and the

average $\Phi_{\text{T}}(B)$ as the anisotropic and isotropic signals, respectively. In all four panels, the isotropic triplet yield has the sigmoidal field dependence typical of a radical pair reaction (44). Magnetic fields comparable to or larger than the hyperfine interactions (~1 mT) suppress the formation of the $\text{T}_{\pm 1}$ triplet radical pair states and so reduce Φ_{T} . As n_{nuc} is increased, the anisotropic triplet yield shrinks across the whole range of applied fields, most markedly at low field (Fig. 1, Insets). For example, in the geomagnetic field (e.g., $B = 50 \mu\text{T}$), the difference between the maximum and minimum values of Φ_{T} is 0.022 for $n_{\text{nuc}} = 2$ (Fig. 1A) falling to 0.0020 for $n_{\text{nuc}} = 5$ (Fig. 1D) and 0.00023 for $n_{\text{nuc}} = 8$ (SI Appendix, section S2). The poor detection sensitivity of the standard model is exacerbated in vivo by the low intensity of the light available to generate the radical pairs on a clear, moonless starry night [~ 3 photons $\text{s}^{-1} \mu\text{m}^{-2}$ (6)].

The only aspect of the magnetic field effects in Fig. 1 that is not strongly attenuated as n_{nuc} is increased is the isotropic effect of fields stronger than ~1 mT. The difference between $\Phi_{\text{T}}(50 \text{ mT})$ and $\Phi_{\text{T}}(0)$ in Fig. 1 is roughly independent of the number of nuclei: 0.20 when $n_{\text{nuc}} = 2$ (Fig. 1A), 0.26 when $n_{\text{nuc}} = 5$ (Fig. 1D), 0.23 when $n_{\text{nuc}} = 8$ and 0.25 when $n_{\text{nuc}} = 14$ (SI Appendix, section S2). Instead of using the tiny *anisotropic* effects of the Earth’s magnetic field as the source of directional information (as in the standard radical pair model), the compass mechanism proposed here relies on the much larger isotropic magnetic field effects expected for magnetic fields between 1 and 10 mT.

Hybrid Radical-Pair/Magnetite Mechanism. With reference to Fig. 2, we consider an ensemble of randomly oriented CRY4a molecules at position \mathbf{r} relative to the center of a single-domain magnetic nanoparticle (MNP) with a remanent magnetic dipole moment $\boldsymbol{\mu}_{\text{MNP}}$. The nanoparticle is assumed to be spherical, with radius R . Both the radical pairs and the nanoparticle experience the geomagnetic field, \mathbf{B}_{GMF} . The dipole is large enough that the magnetic energy, $\boldsymbol{\mu}_{\text{MNP}} \cdot \mathbf{B}_{\text{GMF}}$, is comparable to the thermal energy, $k_{\text{B}} T$, at physiological temperature so that $\boldsymbol{\mu}_{\text{MNP}}$ tends to align with \mathbf{B}_{GMF} provided the nanoparticle is free to rotate and has no preferred orientation in the absence of an external magnetic field. Any change in the angle, θ , between \mathbf{B}_{GMF} and \mathbf{r} therefore changes the average direction of $\boldsymbol{\mu}_{\text{MNP}}$ relative to \mathbf{r} . The radical pairs therefore experience a magnetic field $\mathbf{B}_{\text{GMF}} + \mathbf{B}_{\text{MNP}}(\mathbf{r})$, where $\mathbf{B}_{\text{MNP}}(\mathbf{r})$ is the fringing field of the nanomagnet:

$$\mathbf{B}_{\text{MNP}}(\mathbf{r}) = \left(\frac{\mu_0}{4\pi} \right) \left(-\frac{\boldsymbol{\mu}_{\text{MNP}}}{r^3} + \frac{3(\boldsymbol{\mu}_{\text{MNP}} \cdot \mathbf{r})\mathbf{r}}{r^5} \right), \quad [1]$$

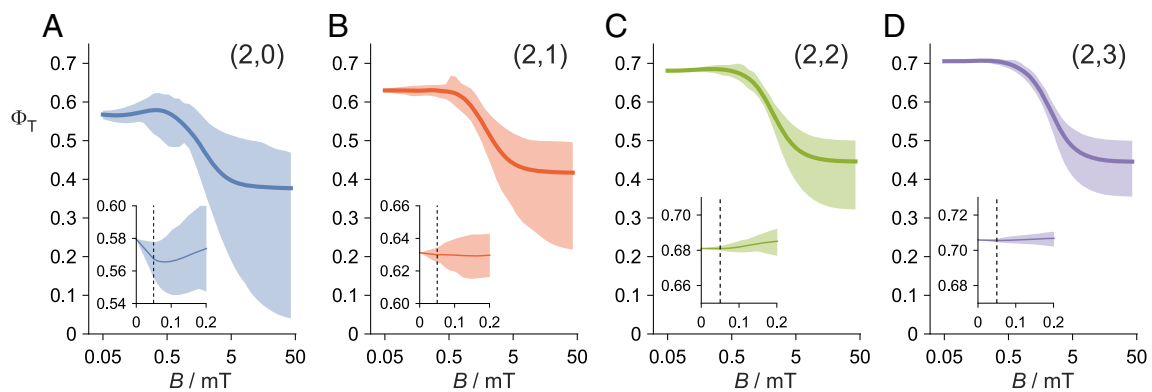


Fig. 1. Magnetic field effects calculated for toy models of the $\text{FAD}^{\bullet-} \text{TrpH}^{\bullet+}$ radical pair in avian CRY4a, with 2 nuclear spins in the flavin radical and (A) 0, (B) 1, (C) 2, and (D) 3 in the tryptophan radical. The four panels show the range (shaded areas) and average values (solid lines) of the triplet product yield for 400 directions of a magnetic field ranging from 0.05 to 50 mT. The four insets, all plotted on the same vertical scale, show the low-field regions (0 to 0.2 mT) with the geomagnetic field (0.05 mT) indicated by dashed lines.

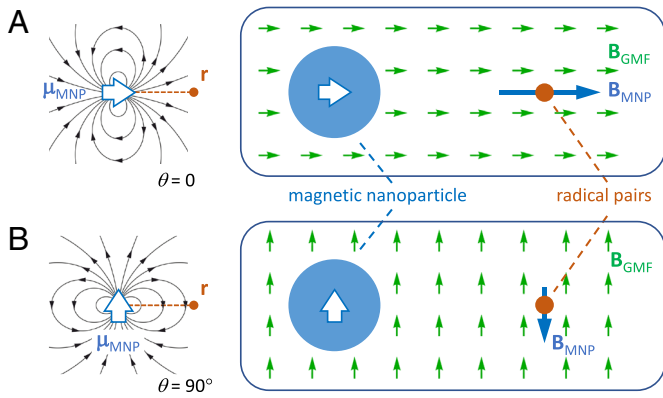


Fig. 2. Schematic operation of the hybrid magnetoreceptor complex. In this illustration, the geomagnetic field, \mathbf{B}_{GMF} (green arrows), and the magnetic dipole moment of the nanoparticle, μ_{MNP} (open blue arrows), are parallel and make an angle θ with the vector, \mathbf{r} , that defines the position of the radical pairs with respect to the center of the nanoparticle. (A) $\theta = 0$ and (B) $\theta = 90^\circ$. \mathbf{B}_{MNP} (solid blue arrows) is the fringing field of the nanomagnet at position \mathbf{r} . The figures on the left-hand side show the lines of magnetic flux for (A) $\theta = 0$ and (B) $\theta = 90^\circ$.

and μ_0 is the vacuum permeability, $4\pi \times 10^{-7} \text{ H m}^{-1}$. When μ_{MNP} is parallel to \mathbf{B}_{GMF} and both are parallel to \mathbf{r} ($\theta = 0$, Fig. 2A), $\mathbf{B}_{\text{MNP}}(\mathbf{r})$ is parallel to \mathbf{B}_{GMF} . When μ_{MNP} and \mathbf{B}_{GMF} are perpendicular to \mathbf{r} ($\theta = 90^\circ$, Fig. 2B), $\mathbf{B}_{\text{MNP}}(\mathbf{r})$ is antiparallel to \mathbf{B}_{GMF} and half the size it was when $\theta = 0$. The magnitude of the net magnetic field at position \mathbf{r} , $|\mathbf{B}_{\text{GMF}} + \mathbf{B}_{\text{MNP}}(\mathbf{r})|$, therefore depends on the direction of \mathbf{B}_{GMF} relative to the nanoparticle–CRY4a axis, \mathbf{r} . The direction of $\mathbf{B}_{\text{GMF}} + \mathbf{B}_{\text{MNP}}(\mathbf{r})$ also depends on θ but that has no relevance here because the radical pairs are randomly oriented so that any anisotropic magnetic field effect will not survive ensemble averaging. If \mathbf{r} is not too large, $\mathbf{B}_{\text{MNP}}(\mathbf{r})$ can be substantially stronger than \mathbf{B}_{GMF} . Thus, the magnetic nanoparticle can be said to amplify \mathbf{B}_{GMF} in a manner that encodes its direction. We refer to the combination of nanomagnetic amplifier and radical-pair sensor in Fig. 2 as the “magnetoreceptor complex.”

To explore the sensitivity of this hybrid magnetoreceptor complex, we model the field dependence of Φ_{T} for the ensemble of CRY4a molecules as a Lorentzian with half-width at half-maximum height, $B_{1/2} = 4 \text{ mT}$ (Fig. 3A):

$$\Phi_{\text{T}}(B) = \Phi_{\text{T}}(\infty) + \frac{\Phi_{\text{T}}(0) - \Phi_{\text{T}}(\infty)}{1 + (B/B_{1/2})^2}. \quad [2]$$

Both the Lorentzian form and this value of $B_{1/2}$ are typical for $\text{FAD}^{\bullet-} \text{TrpH}^{\bullet+}$ radical pairs in purified avian CRY4a (14, 19, 20). The magnitude of the magnetic field effect is determined by the values of $\Phi_{\text{T}}(0)$ and $\Phi_{\text{T}}(\infty)$ (Fig. 3A). For reasons that will shortly become clear, we use $\Phi_{\text{T}}(0) = 0.73$ and $\Phi_{\text{T}}(\infty) = 0.48$.

We consider the nanoparticle to be composed of magnetite with a saturation magnetization, $M_{\text{S}} = 4.8 \times 10^5 \text{ A m}^{-1}$ (37), and magnetic dipole moment, $\mu_{\text{MNP}} = (4\pi R^3/3)M_{\text{S}}$. The condition for μ_{MNP} to be significantly aligned with the geomagnetic field is $\eta = \mu_{\text{MNP}}B_{\text{GMF}}/k_{\text{B}}T > 1$. When $B_{\text{GMF}} = 50 \mu\text{T}$ and $T = 40^\circ\text{C}$ (physiological temperature), $\eta > 1$ when $\mu_{\text{MNP}} > 0.086 \text{ fA m}^2$ and hence when the particle radius, R , is greater than 35 nm.

For the purposes of the proposed detection scheme, the magnetic fields experienced by the radical pairs should correspond to the part of Fig. 3A where $\Phi_{\text{T}}(B)$ has the strongest dependence on B , i.e. $1 < B < 10 \text{ mT}$. If μ_{MNP} were aligned perfectly with \mathbf{B}_{GMF} (i.e., when $\eta \gg 1$), this would occur at a position $r \approx 4R$ where

$3.14 \leq B_{\text{MNP}}(\mathbf{r}) \leq 6.28 \text{ mT}$, depending on the direction of \mathbf{B}_{GMF} and therefore μ_{MNP} . Under these conditions, the magnetic field at the position of the radical pairs would be $60B_{\text{GMF}}$ to $120B_{\text{GMF}}$ independent of R . For smaller values of η , μ_{MNP} is less well aligned with \mathbf{B}_{GMF} and the net magnetic field at \mathbf{r} is an average, $\langle \dots \rangle$, over the distribution of μ_{MNP} directions:

$$\langle B_{\text{total}}(r, \theta) \rangle = \langle |\mathbf{B}_{\text{GMF}} + \mathbf{B}_{\text{MNP}}(\mathbf{r})| \rangle, \quad [3]$$

(SI Appendix, section S3). Fig. 3B shows the dependence of $\langle B_{\text{total}}(4R, \theta) \rangle$ on θ , for five nanoparticle radii. In all five cases, $\langle B_{\text{total}}(r, \theta) \rangle$ is substantially larger than B_{GMF} , with the larger nanoparticles producing a stronger orientation dependence because of the greater alignment of μ_{MNP} with \mathbf{B}_{GMF} .

Using Eq. 2, Fig. 3C shows the dependence of the averaged triplet yield, $\langle \Phi_{\text{T}}(B_{\text{total}}(4R, \theta)) \rangle$, on θ under the conditions of Fig. 3B. The triplet yield depends on the direction of \mathbf{B}_{GMF} for the same reason that $\langle B_{\text{total}}(4R, \theta) \rangle$ does. Fig. 3B and C resemble one another because $\Phi_{\text{T}}(B)$ is approximately linear in B in the relevant field range (3.14 to 6.28 mT, Fig. 3A).

The dependence of $\langle \Phi_{\text{T}} \rangle$ on the direction of \mathbf{B}_{GMF} (i.e., on θ) is assumed to provide the signal from which a bird could derive a magnetic compass bearing. This quantity, defined here as

$$\Delta\Phi_{\text{T}} = \langle \Phi_{\text{T}}(B_{\text{total}}(r, 90^\circ)) \rangle - \langle \Phi_{\text{T}}(B_{\text{total}}(r, 0)) \rangle, \quad [4]$$

is plotted against r in Fig. 3D using the same nanoparticle radii as in Fig. 3B and C. As R and therefore μ_{MNP} are increased, μ_{MNP} is more closely aligned with \mathbf{B}_{GMF} , and the signal, $\Delta\Phi_{\text{T}}$, increases. The maxima in Fig. 3D occur at roughly four times the nanoparticle radii as anticipated above. As shown in Fig. 3E, $\Delta\Phi_{\text{T}}$ is not strongly dependent on $B_{1/2}$: As the width of the field-dependence (Fig. 3A) is increased, the radical pairs need to be closer to the nanoparticle to achieve the maximum $\Delta\Phi_{\text{T}}$. Fig. 3D–F were drawn for specific values of $\Phi_{\text{T}}(0)$ and $\Phi_{\text{T}}(\infty)$ but can easily be generalized using the proportionality between $\Delta\Phi_{\text{T}}$ and $\Phi_{\text{T}}(0) - \Phi_{\text{T}}(\infty)$ (Eqs. 2 and 4).

Finally, Fig. 3F shows how $\Delta\Phi_{\text{T}}^{\text{max}}$, the maximum value of $\Delta\Phi_{\text{T}}$ (e.g. in Fig. 3D), varies with the magnetic dipole moment of the nanoparticle. As μ_{MNP} is increased, μ_{MNP} becomes more closely aligned with \mathbf{B}_{GMF} and so $\Delta\Phi_{\text{T}}^{\text{max}}$ increases. Once μ_{MNP} is greater than $\sim 1 \text{ fA m}^2$, the alignment is almost perfect, and the signal reaches a plateau ($\Delta\Phi_{\text{T}}^{\text{max}} = 0.17$, SI Appendix, section S3).

Discussion

The potential sensitivity enhancement of this hybrid compass relative to the standard model can be estimated by means of spin dynamics simulations of $\text{FAD}^{\bullet-} \text{TrpH}^{\bullet+}$ (SI Appendix, section S2). Including the 14 nuclear spins with the largest hyperfine interactions (7 in $\text{FAD}^{\bullet-}$ and 7 in $\text{TrpH}^{\bullet+}$), the anisotropy of the reaction yield in a 50- μT magnetic field is 8.5×10^{-5} in the standard model. To obtain the corresponding figure for the hybrid model, we first determined the isotropic triplet yield in zero field and in a magnetic field much stronger than the hyperfine interactions: $\Phi_{\text{T}}(0) = 0.73$, $\Phi_{\text{T}}(\infty) = 0.48$, and hence $\Phi_{\text{T}}(0) - \Phi_{\text{T}}(\infty) = 0.25$ (SI Appendix, section S2). These are precisely the values that were used for Fig. 3A–F. Therefore, we can simply read off from Fig. 3F the maximum signal for a $R = 50 \text{ nm}$ spherical nanoparticle ($\mu_{\text{MNP}} = 0.25 \text{ fA m}^2$) as $\Delta\Phi_{\text{T}}^{\text{max}} = 0.030$. The estimated sensitivity gain of the hybrid model over the standard model is therefore $0.03/(8.5 \times 10^{-5}) = 350$. The corresponding enhancements for $R = 40, 30, \text{ and } 20 \text{ nm}$ ($\mu_{\text{MNP}} = 0.13, 0.054, \text{ and } 0.016 \text{ fA m}^2$)

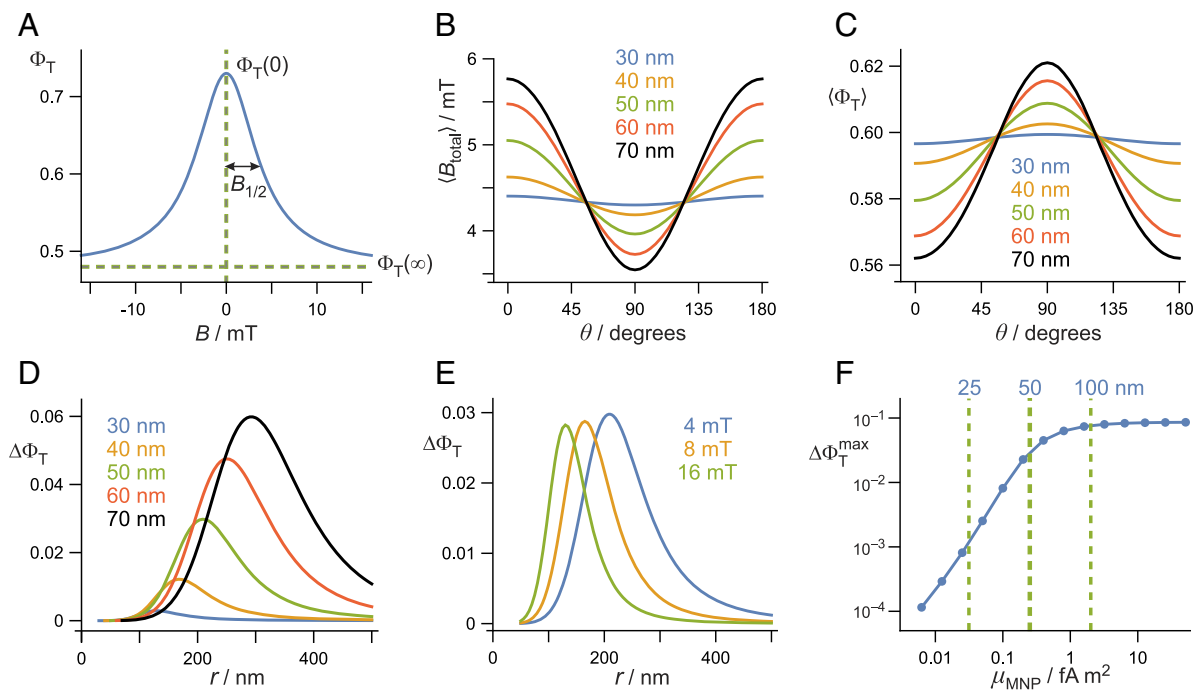


Fig. 3. (A) Magnetic field dependence of the triplet product yield, Eq. 2, with $\Phi_T(0) = 0.73$, $\Phi_T(\infty) = 0.48$, $B_{1/2} = 4$ mT. These values were used for all six panels with the exception of $B_{1/2}$ in panel (E). (B) Dependence of the averaged magnetic field, Eq. 3, experienced by radical pairs positioned at $r = 4R$ (with $R = 30$ to 70 nm), on the angle between the geomagnetic field and the vector \mathbf{r} . (C) Averaged triplet yields under the conditions of panel (B). (D) Dependence of $\Delta\Phi_T$, Eq. 4, on the distance of the radical pairs from a magnetic nanoparticle of radius $R = 30$ to 70 nm. (E) Dependence of $\Delta\Phi_T$, Eq. 4, on the distance of the radical pairs from a magnetic nanoparticle of radius $R = 50$ nm, with $B_{1/2} = 4, 8, 16$ mT. (F) Dependence of the maximum $\Delta\Phi_T$ on the magnetic dipole moment of the nanoparticle. The dashed lines indicate the values of μ_{MNP} for spherical particles of radius $R = 25, 50, 100$ nm. Details of all these calculations are given in the *SI Appendix, section S3*.

are 140, 34, and 4.9. When $\mu_{\text{MNP}} > 1$ fA m², the alignment of μ_{MNP} with \mathbf{B}_{GMF} is almost perfect (Fig. 3F) and the enhancement plateaus at just over 1,000. These potential improvements in sensitivity could be even larger given the differential effects of spin relaxation at high and low field, which were excluded from these simulations (*SI Appendix, section S4*).

It is currently impossible to derive an alternative estimate of the sensitivity gain using exclusively experimental data because no anisotropic magnetic field effects at 50 μT have yet been measured for any cryptochrome. However, an approximate value can be obtained from the 8% isotropic magnetic field effect reported for European robin CRY4a (14). Taking $\Phi_T(0) = 0.73$, as above, an 8% effect corresponds to $\Phi_T(0) - \Phi_T(\infty) \approx 0.06$, i.e., 4.2 times smaller than the value (0.25) obtained from the simulations mentioned in the last paragraph. Since $\Delta\Phi_T$ is proportional to $\Phi_T(0) - \Phi_T(\infty)$, we can estimate a sensitivity enhancement of $350/4.2 \approx 80$ for a $R = 50$ nm nanoparticle. This result may also be an underestimate because the attenuating effects of spin relaxation are included in the experimentally measured (8%) magnetic field effect but not in the standard-model simulations.

To put these estimates in context, an N -fold increase in the signal strength translates to an N^2 -fold reduction in the number of radical pairs required to achieve a compass bearing with a given precision (e.g., to within 5° , *SI Appendix, section S5*) (21, 45). A hybrid compass could therefore function satisfactorily with fewer radical pairs, and therefore lower light intensities, than a standard-model compass. A rough estimate of the number of photons that enter the double-cone photoreceptor cells in a songbird's eye on a clear, moonless, star-lit night is $\sim 2 \times 10^8 \text{ min}^{-1}$ (21). Assuming the ~ 350 -fold enhancement estimated above, this number is roughly 1,000 times more than would be required for a precision of 5° using a hybrid compass and about 100 times too

few if using a standard-model compass. *SI Appendix, sections S6 and S7* summarize the origins of the sensitivity differences between the two models.

Previous discussions of the effects of nanomagnets on radical pair reactions have concentrated on singlet-triplet interconversion driven by the gradient of the fringing field (33, 34). Such effects are not expected to be important here (*SI Appendix, section S8*).

Despite their differences, the two models have a number of important aspects in common. The hybrid model still requires blue light to excite the cryptochrome and, like the standard model, is an inclination compass (1, 26). Although the direction of the total field experienced by the radical pairs changes when \mathbf{B}_{GMF} is inverted, its magnitude does not and, as explained above, it is the strength of the total field that encodes the direction of \mathbf{B}_{GMF} . The two models both assume that the compass bearing is transduced via a signaling state of the protein interacting with partner proteins to initiate a signal transduction cascade with biochemical amplification. In principle, both models are compatible with the proposed “dark” radical pair, $\text{FADH}^\bullet \text{O}_2^{\bullet-}$ (41, 42), but only if Nature has found a way to circumvent the extremely fast spin relaxation of the superoxide radical (43).

An essential feature of the standard model is that the cryptochromes in each cell should be mutually aligned (25, 45). Throughout the avian retina, CRY4a is found in the outer segments of the long-wavelength and double-cone photoreceptor cells (17, 46), the latter being a favorable location for a magnetic direction sensor. Approximately cylindrical and pointing toward the pupil, the outer segments of the double cones are packed with oriented membranes carrying visual pigment proteins (iodopsins) to which the cryptochromes could be tethered, and thereby aligned and immobilized (17). Double cones at different locations in the approximately hemispherical retina have

different orientations and should therefore have different but correlated responses to the geomagnetic field. Processing of signals from cells distributed across the retina should improve signal-to-noise and provide the information the bird would need to determine a magnetic compass bearing (21, 45). The same principles apply in the hybrid model except that it is the magnetoreceptor complexes that must be aligned within the cells so that cells at different locations once again transduce correlated directional information. Although the cryptochromes must not be uniformly distributed around the nanomagnet, they do not have to be located at a precise distance from it. For example, if the CRY4a molecules occupy a spherical region with radius 50 nm, centered 210 nm away from a $R = 50$ nm nanoparticle, $\Delta\Phi_T$ would be 89% of its value when all the sensors are localized at 210 nm. This percentage drops to 66% if the CRY4a “pool” has a radius of 100 nm (*SI Appendix, section S9*). Thus, it is not crucial for all the sensors to have the same distance from the amplifier within the magnetoreceptor complex. Although we have presented the hybrid model in terms of randomly oriented CRY4a molecules, it would work just as well if the proteins were partially aligned via their interactions with membrane proteins. Each cell could contain several magnetoreceptor complexes for improved signal-to-noise.

A potential difficulty with both models is that the fraction of the cryptochrome molecules present in the signaling state in a cell will depend much more strongly on the intensity and possibly polarization of the incoming light than on the direction of the geomagnetic field experienced by the cell (47). A possible solution to this problem is to compare the signals from nearest neighbor cells which would experience the same photon flux but would have different magnetic responses (47). Variations in both light intensity and polarization could be canceled if adjacent cells were differentially rotated around the retina normal. Subsequently, it was found that the double cones form an oriented mosaic that could enable just such a cancelation to occur (46). This mechanism, derived with the standard model in mind, should apply equally well to the hybrid model provided the magnetite-CRY4a vector \mathbf{r} has a component perpendicular to the rotation axis of the cells.

As argued above, a hybrid magnetite-cryptochrome magnetic compass offers a major sensitivity advantage. On the basis of Fig. 3F, the hybrid design would deliver directional signals 10 to 100 times larger than the standard model if the nanoparticle had a magnetic dipole moment in the range 0.03 to 0.10 fA m², corresponding to a radius of 20 to 40 nm for a spherical nanomagnet or to a length of 60 to 100 nm for a cuboidal particle with length/width ratio equal to 2. These dimensions fall within the range in which magnetite crystals are expected to be single-domain rather than superparamagnetic or multidomain (48). They are also comparable to the single-domain magnetite crystals found in biological tissue [typically ~50 nm (49)] and to the intracellular magnetite crystals contained in the magnetosomes of magnetotactic bacteria [typically 30 to 140 nm (50)]. An enhancement greater than ~500 would require a magnetic dipole moment (>0.4 fA m²) outside the normal range for single-domain magnetite crystals. Such large magnetic moments might arise from compact clusters of several smaller crystals (51).

Although there seem to be no confirmed reports of intracellular magnetite crystals in the avian retina, small magnetite particles may have escaped detection. An extensive study, using rotating magnetic fields to detect spinning cells, revealed no biogenic magnetite in pigeon tissue (52). However, this assay would not have been sensitive to particles with the relatively small magnetic

moments (<1 fA m², Fig. 3F) needed for the hybrid model. Moreover, cells containing the loosely anchored magnetite crystals required here, would not have been induced to spin whatever their magnetic moments.

In addition to a sufficient magnetic moment, the other main requirement for the nanoparticle is that it is able to rotate relatively freely into alignment with the Earth's magnetic field. Its rotational motion should therefore not be constrained by attachment to cellular structures [as required in an earlier hybrid compass proposal (36)]. A simple treatment of the magnetic and viscous torques experienced by a spherical magnetic particle suspended in an isotropic fluid (53) suggests that the characteristic time taken to align with the Earth's field is independent of the particle radius, proportional to viscosity, and equal to ~200 μ s for water at 40 °C (*SI Appendix, section S10*). Even if the surrounding medium had ten times the viscosity of water, alignment would be complete within ~10 ms. It seems unlikely that a bird would need to determine a compass bearing more rapidly than that. Indeed, it could be advantageous, for signal-to-noise reasons, to integrate or otherwise accumulate directional information for much longer periods (e.g. ~1 min) (21, 45).

Perhaps the most serious piece of evidence against this hybrid compass mechanism in migratory songbirds is that it is incompatible with recent behavioral tests using radiofrequency magnetic fields superimposed on the geomagnetic field. The finding that Eurasian blackcaps were unable to use their magnetic compass when subjected to (~ 1 pT/ $\sqrt{\text{Hz}}$) broadband magnetic noise in the frequency bands 1 to 10 MHz and 80 \pm 5 MHz (54) but were unaffected by 140 \pm 5 MHz and 240 \pm 5 MHz fields of similar intensity (55) is qualitatively consistent with the standard radical pair hypothesis in which a FAD^{•-}-containing radical pair acts as the sensor. This conclusion was based on the calculated maximum frequency of singlet-triplet interconversion in the FAD^{•-} TrpH^{•+} radical pair (116 MHz) which is the predicted threshold between disorientation at lower frequencies and no effect at higher frequencies (55, 56). A hybrid compass, in which the radicals experience a static magnetic field approximately 100 times stronger than the geomagnetic field, would have faster singlet-triplet spin dynamics and therefore a higher threshold for radiofrequency disorientation that would be inconsistent with the behavioral tests (*SI Appendix, section S11*). However, it would be premature to dismiss the possibility of a hybrid compass mechanism given that the standard model is quantitatively unable to account for the disorientation caused by radiofrequency fields predicted to be at least 1,000 times too weak to produce significant changes in the yield of a cryptochrome signaling state (56).

Finally, how could a hybrid direction sensor be distinguished from one based on the standard model? Short, intense magnetic-field pulses have been extensively used in behavioral tests as a diagnostic for magnetite-based magnetic sensors (57–64). However, the hybrid sensor proposed here should not be affected by pulsed magnetic fields because it relies on a single untethered magnetite crystal rather than a chain of interacting particles attached to a cytoskeletal structure. If the experiment involves a static, biasing magnetic field (61–63), the nanoparticle would rotate to align its magnetic moment with the field. A strong magnetic pulse parallel to the bias field should then have no effect while an antiparallel field should invert the magnetic moment of the particle. As soon as the two magnetic fields are switched off, however, the particle would quickly rotate so that its magnetic moment aligns once more with the Earth's magnetic field. The net change to the particle would be zero. The same would be true if the test were performed without a bias field.

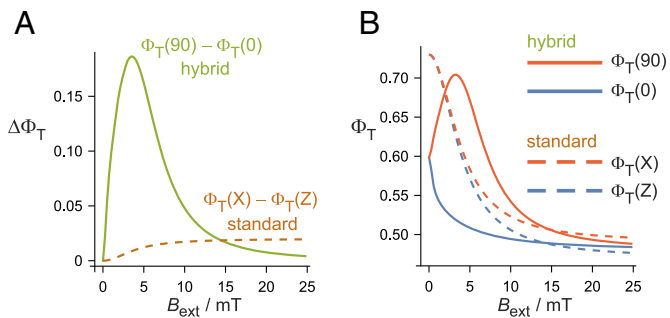


Fig. 4. Dependence of (A) $\Delta\Phi_T$ and (B) Φ_T for the standard and hybrid models on the strength of an external magnetic field, B_{ext} . For the hybrid model, $\Delta\Phi_T$ is the difference between $\Phi_T(\theta = 90^\circ)$ and $\Phi_T(\theta = 0)$ (Eq. 4 and Fig. 2). For the standard model, $\Delta\Phi_T = \Phi_T(X) - \Phi_T(Z)$, where X and Z indicate the direction of the external field relative to the axis system of the flavin radical (SI Appendix, section S2). All calculations use Eq. 2 with $\Phi_T(0) = 0.73$ and $B_{1/2} = 4$ mT. $\Phi_T(\infty) = 0.48$ (hybrid model), 0.49 (standard model, X), or 0.47 (standard model, Z). $R = 25$ nm and $r = 4R$. Hybrid sensors with different nanoparticle radii (R) have the $\Delta\Phi_T$ -maximum at similar values of B_{ext} (3 to 4 mT).

More promising approaches are suggested by the predicted responses of the two sensors to external magnetic fields, B_{ext} , stronger than the Earth's. Fig. 4A compares the directional signals ($\Delta\Phi_T$) expected for the two models as a function of B_{ext} . The standard model shows the sigmoidal dependence characteristic of radical pair reactions, leveling out when B_{ext} exceeds $B_{1/2}$. By contrast, a hybrid sensor, based on the same radical pairs, is predicted to have a peaked response with a pronounced maximum at 3 to 4 mT. The origin of this striking difference can be seen from the signals (Φ_T) predicted for orthogonal external magnetic fields, shown Fig. 4B. Note that each of the $\Delta\Phi_T$ traces in Fig. 4A is the difference between the corresponding parallel and perpendicular traces in Fig. 4B. In the case of the standard sensor, the signals for applied fields parallel and perpendicular to the flavin Z-axis are rather similar, reflecting the relatively small anisotropy afforded by the hyperfine interactions (Fig. 1 and SI Appendix, section S2). For the hybrid model, when B_{ext} is parallel to the vector \mathbf{r} ($\theta = 0$), the field generated by the nanoparticle, B_{MNP} , is roughly parallel to B_{ext} so that the proteins experience a net field stronger than B_{ext} (geometry as in Fig. 2A). Conversely, when B_{ext} is perpendicular to \mathbf{r} ($\theta = 90^\circ$), B_{MNP} is antiparallel to B_{ext} and

the net field at the position of the cryptochromes is smaller than B_{ext} (geometry as in Fig. 2B). The form of Fig. 4 can then be understood by noting that smaller net fields correspond to larger Φ_T (Fig. 3A).

The pronounced difference in the signals predicted for the two types of sensor in the range $1 \text{ mT} \leq B_{\text{ext}} \leq 10 \text{ mT}$ (Fig. 4A) should allow the mechanisms to be distinguished. One possibility could be to use in vivo or ex vivo electrophysiology (65–68). However, previous attempts to detect a dependence of neuronal activity on the direction of the geomagnetic field were either irreproducible or have yet to be independently replicated. A more promising approach would be two-photon calcium imaging (69–71), again in vivo or ex vivo. Such methods would not suffer from the magnetically induced electrical artefacts which have bedeviled electrophysiological recordings. Finally, it should be possible to adapt the fluorescence-based methods that have been used to detect magnetic field effects on purified cryptochromes (14, 20, 72, 73) for measurements on the photoreceptor cells that appear to contain the magnetoreceptors. The difficulties of using behavioral tests to distinguish the two models are discussed briefly in the SI Appendix, section S12.

Materials and Methods

The toy-model data in Fig. 1 were calculated as described in ref. 74. Calculations for two larger models of the flavin-tryptophan radical pair were performed using the MolSpin package (24, 75), either by exactly solving the Liouville-von Neumann equation ($n_{\text{nuc}} = 8$) (75) or by using the stochastic Schrödinger equation method ($n_{\text{nuc}} = 14$) (24, 75, 76). Hyperfine interactions were taken from the Supplementary Information of Ref. 44. See SI Appendix, sections S1 and S2 for further details. Eqs. 1–4 were used to produce the data in Figs. 3 and 4, as described in the Results and in SI Appendix, section S3.

Data, Materials, and Software Availability. All study data are included in the article and/or SI Appendix.

ACKNOWLEDGMENTS. I am grateful to Hannah Lonergan née Hogben and Laura Kane for preliminary work, to Luca Gerhards for the $n_{\text{nuc}} = 8$ and $n_{\text{nuc}} = 14$ spin dynamics simulations, to the European Research Council (Synergy Grant, QuantumBirds, grant agreement 810002, under the European Union's Horizon 2020 research and innovation programme) and the Deutsche Forschungsgemeinschaft (Magnetoreception and navigation in vertebrates, SFB 1372, project no. 395940726).

- R. Wiltschko, W. Wiltschko, *Magnetic Orientation in Animals* (Springer Verlag, Berlin, 1995).
- H. Mouritsen, Long-distance navigation and magnetoreception in migratory animals. *Nature* **558**, 50–59 (2018).
- S. Nimpf, D. A. Keays, Myths in magnetosensation. *iScience* **25**, 104454 (2022).
- G. C. Nordmann, T. Hochstoeger, D. A. Keays, Magnetoreception – A sense without a receptor. *PLoS Biol.* **15**, e2003234 (2017).
- T. Ritz, S. Adem, K. Schulten, A model for photoreceptor-based magnetoreception in birds. *Biophys. J.* **78**, 707–718 (2000).
- P. J. Hore, H. Mouritsen, The radical pair mechanism of magnetoreception. *Annu. Rev. Biophys.* **45**, 299–344 (2016).
- J. Shaw *et al.*, Magnetic particle-mediated magnetoreception. *J. R. Soc. Interface* **12**, 20150499 (2015).
- M. Winklhofer, J. L. Kirschvink, A quantitative assessment of torque-transducer models for magnetoreception. *J. Roy. Soc. Interface* **7**, S273–S289 (2010).
- P. J. Hore, Magneto-oncology: A radical pair primer. *Front. Oncol.* **15**, 1539718 (2025).
- N. Ozturk *et al.*, Comparative photochemistry of animal type 1 and type 4 cryptochromes. *Biochemistry* **48**, 8585–8593 (2009).
- H. Mitsui *et al.*, Overexpression in yeast, photocycle, and in vitro structural change of an avian putative magnetoreceptor cryptochrome 4. *Biochemistry* **54**, 1908–1917 (2015).
- B. D. Zoltowski *et al.*, Chemical and structural analysis of a photoactive vertebrate cryptochrome from pigeon. *Proc. Natl. Acad. Sci. U.S.A.* **116**, 19449–19457 (2019).
- T. Hochstoeger *et al.*, The biophysical, molecular, and anatomical landscape of pigeon CRY4: A candidate light-based quantum magnetosensor. *Sci. Adv.* **6**, eabb9110 (2020).
- J. Xu *et al.*, Magnetic sensitivity of cryptochrome 4 from a migratory songbird. *Nature* **594**, 535–540 (2021).
- H. Otsuka *et al.*, Rapid oxidation following photoreduction in the avian cryptochrome 4 photocycle. *Biochemistry* **59**, 3615–3625 (2020).
- D. Timmer *et al.*, Tracking the electron transfer cascade in European robin cryptochrome 4 mutants. *J. Am. Chem. Soc.* **145**, 11566–11578 (2023).
- A. Günther *et al.*, Double-cone localization and seasonal expression pattern suggest a role in magnetoreception for European robin cryptochrome 4. *Curr. Biol.* **28**, 211–223 (2018).
- Y. Vortman, R. Fitak, E. Natan, Magnetoreception and the ruling hypothesis. *J. Exp. Biol.* **228**, jeb250252 (2025).
- M. Golezworthy *et al.*, Singlet-triplet dephasing in radical pairs in avian cryptochromes leads to time-dependent magnetic field effects. *J. Chem. Phys.* **159**, 105102 (2023).
- J. Gravell *et al.*, Spectroscopic characterisation of radical pair photochemistry in nonmigratory avian cryptochromes: Magnetic field effects in GgCry4a. *J. Am. Chem. Soc.* **147**, 24286–24298 (2025).
- H. G. Hiscock *et al.*, Navigating at night: Fundamental limits on the sensitivity of radical pair magnetoreception under dim light. *Q. Rev. Biophys.* **52**, e9 (2019).
- N. S. Babcock, D. R. Kattinig, Electron-electron dipolar interaction poses a challenge to the radical pair mechanism of magnetoreception. *J. Phys. Chem. Lett.* **11**, 2414–2421 (2020).
- D. R. Kattinig, I. A. Solov'yov, P. J. Hore, Electron spin relaxation in cryptochrome-based magnetoreception. *Phys. Chem. Chem. Phys.* **18**, 12443–12456 (2016).
- L. Gerhards, C. Nielsen, D. R. Kattinig, P. J. Hore, I. A. Solov'yov, Modeling spin relaxation in complex radical systems using MolSpin. *J. Comput. Chem.* **44**, 1704–1714 (2023).
- J. C. S. Lau, N. Wagner-Rundell, C. T. Rodgers, N. J. B. Green, P. J. Hore, Effects of disorder and motion in a radical pair magnetoreceptor. *J. Roy. Soc. Interface* **7**, S257–S264 (2010).
- P. L. Benjamin, L. Gerhards, I. A. Solov'yov, P. J. Hore, Magnetosensitivity of model flavin-tryptophan radical pairs in a dynamic protein environment. *J. Phys. Chem. B* **129**, 5937–5947 (2025).
- P. Herve, F. Nome, J. H. Fendler, Magnetic effects on chemical-reactions in the absence of magnets – Effects of surfactant vesicle entrapped magnetite particles on benzophenone photochemistry. *J. Am. Chem. Soc.* **106**, 8291–8292 (1984).
- J. C. Scaiano, S. Monahan, J. Renaud, Dramatic effect of magnetite particles on the dynamics of photogenerated free radicals. *Photochem. Photobiol.* **65**, 759–762 (1997).

29. C. F. Chignell, R. H. Sik, Effect of magnetite particles on photoinduced and nonphotoinduced free radical processes in human erythrocytes. *Photochem. Photobiol.* **68**, 598–601 (1998).
30. N. Yang, A. E. Cohen, Optical imaging through scattering media via magnetically modulated fluorescence. *Opt. Express* **18**, 25461–25467 (2010).
31. H. Lee, N. Yang, A. E. Cohen, Mapping nanomagnetic fields using a radical pair reaction. *Nano Lett.* **11**, 5367–5372 (2011).
32. N. G. Chalkias, P. Kahawong, E. P. Giannelis, Activity increase of horseradish peroxidase in the presence of magnetic particles. *J. Am. Chem. Soc.* **130**, 2910–2911 (2008).
33. A. E. Cohen, Nanomagnetic control of intersystem crossing. *J. Phys. Chem. A* **113**, 11084–11092 (2009).
34. J. Cai, Quantum probe and design for a chemical compass with magnetic nanostructures. *Phys. Rev. Lett.* **106**, 100501 (2011).
35. Y. Lü, T. Song, Avian magnetoreception model realized by coupling a magnetite-based mechanism with a radical-pair-based mechanism. *Chin. Phys. B* **22**, 048701 (2013).
36. V. N. Binhi, Stochastic dynamics of magnetosomes and a mechanism of biological orientation in the geomagnetic field. *Bioelectromagnetics* **27**, 58–63 (2006).
37. V. Binhi, Do naturally occurring magnetic nanoparticles in the human body mediate increased risk of childhood leukaemia with EMF exposure? *Int. J. Radiat. Biol.* **84**, 569–579 (2008).
38. S. B. Worster, P. J. Hore, Proposal to use superparamagnetic nanoparticles to test the role of cryptochrome in magnetoreception. *J. R. Soc. Interface* **15**, 20180587 (2018).
39. K. Kavokin, Can a hybrid chemical-ferromagnetic model of the avian compass explain its outstanding sensitivity to magnetic noise? *PLoS ONE* **12**, e0173887 (2017).
40. S. Qin *et al.*, A magnetic protein biocompass. *Nat. Mater.* **15**, 217–226 (2016).
41. C. Niessner, S. Denzau, L. Peichl, W. Wiltschko, R. Wiltschko, Magnetoreception: Activation of avian cryptochrome 1a in various light conditions. *J. Comp. Physiol. A* **204**, 977–984 (2018).
42. R. Wiltschko, M. Ahmad, C. Niessner, D. Gehring, W. Wiltschko, Light-dependent magnetoreception in birds: The crucial step occurs in the dark. *J. R. Soc. Interface* **13**, 20151010 (2016).
43. T. C. Player, P. J. Hore, Viability of superoxide-containing radical pairs as magnetoreceptors. *J. Chem. Phys.* **151**, 225101 (2019).
44. S. Y. Wong, P. Benjamin, P. J. Hore, Magnetic field effects on radical pair reactions: Estimation of B_{12} for flavin-tryptophan radical pairs in cryptochromes. *Phys. Chem. Chem. Phys.* **25**, 975–982 (2023).
45. Y. Ren, H. Hiscock, P. J. Hore, Angular precision of radical pair compass magnetoreceptors. *Biophys. J.* **120**, 547–555 (2021).
46. R. Chetverikova, G. Dautaj, L. Schwigon, K. Dedek, H. Mouritsen, Double cones in the avian retina form an oriented mosaic which might facilitate magnetoreception and/or polarized light sensing. *J. R. Soc. Interface* **19**, 20210877 (2022).
47. S. Worster, H. Mouritsen, P. J. Hore, A light-dependent magnetoreception mechanism insensitive to light intensity and polarization. *J. Roy. Soc. Interface* **14**, 20170405 (2017).
48. J. L. Kirschvink, M. M. Walker, "Particle size considerations for magnetite based magnetoreceptors" in *Magnetite biomineralization and magnetoreception in organisms: A new biomagnetism*, J. L. Kirschvink, D. S. Jones, B. J. McFadden, Eds. (Plenum Press, New York, 1985), pp. 243–254.
49. G. Kletetschka, R. Bazala, Magnetite particle size and spatial distribution may modulate neural oscillation in the human brain. *Sci. Rep.* **15**, 21909 (2025).
50. D. Faivre, D. Schuler, Magnetotactic bacteria and magnetosomes. *Chem. Rev.* **108**, 4875–4898 (2008).
51. S. H. K. Eder *et al.*, Magnetic characterization of isolated candidate vertebrate magnetoreceptor cells. *Proc. Natl. Acad. Sci. U.S.A.* **109**, 12022–12027 (2012).
52. N. B. Edelman *et al.*, No evidence for intracellular magnetite in putative vertebrate magnetoreceptors identified by magnetic screening. *Proc. Natl. Acad. Sci. U.S.A.* **112**, 262–267 (2015).
53. K. Erglis *et al.*, Dynamics of magnetotactic bacteria in a rotating magnetic field. *Biophys. J.* **93**, 1402–1412 (2007).
54. B. Leberecht *et al.*, Broadband 75–85 MHz radiofrequency fields disrupt magnetic compass orientation in night-migratory songbirds consistent with a flavin-based radical pair magnetoreceptor. *J. Comp. Physiol. A* **208**, 97–106 (2022).
55. B. Leberecht *et al.*, Upper bound for broadband radiofrequency field disruption of magnetic compass orientation in night-migratory songbirds. *Proc. Natl. Acad. Sci. U.S.A.* **120**, 2301153120 (2023).
56. H. G. Hiscock, H. Mouritsen, D. E. Manolopoulos, P. J. Hore, Disruption of magnetic compass orientation in migratory birds by radiofrequency electromagnetic fields. *Biophys. J.* **113**, 1475–1484 (2017).
57. A. J. Kalmijn, R. P. Blakemore, "The magnetic behavior of mud bacteria" in *Animal Migration, Navigation and Homing*, K. Schmidt-Koenig, W. T. Keeton, Ed. (Springer, Berlin, Germany, 1978), pp. 354–355.
58. W. Wiltschko, U. Munro, R. C. Beason, H. Ford, R. Wiltschko, A magnetic pulse leads to a temporary deflection in the orientation of migratory birds. *Experientia* **50**, 697–700 (1994).
59. R. C. Beason, N. Dussourd, M. E. Deutschlander, Behavioral evidence for the use of magnetic material in magnetoreception by a migratory bird. *J. Exp. Biol.* **198**, 141–146 (1995).
60. R. C. Beason, R. Wiltschko, W. Wiltschko, Pigeon homing: Effects of magnetic pulses on initial orientation. *Auk* **114**, 405–415 (1997).
61. R. A. Holland, J. L. Kirschvink, T. G. Doak, M. Wikelski, Bats use magnetite to detect the Earth's magnetic field. *PLoS ONE* **3**, e1676 (2008).
62. R. A. Holland, Differential effects of magnetic pulses on the orientation of naturally migrating birds. *J. Roy. Soc. Interface* **7**, 1617–1625 (2010).
63. R. A. Holland, B. Helm, A strong magnetic pulse affects the precision of departure direction of naturally migrating adult but not juvenile birds. *J. R. Soc. Interface* **10**, 20121047 (2013).
64. R. A. Holland, True navigation in birds: From quantum physics to global migration. *J. Zool.* **293**, 1–15 (2014).
65. P. Semm, C. Demaine, Neurophysiological properties of magnetic cells in the pigeons visual-system. *J. Comp. Physiol. A* **159**, 619–625 (1986).
66. L. Q. Wu, J. D. Dickman, Neural correlates of a magnetic sense. *Science* **336**, 1054–1057 (2012).
67. M. T. Ahlers, C. T. Block, M. Winklhofer, M. Greschner, Integration and evaluation of magnetic stimulation in physiology setups. *PLoS ONE* **17**, e0271765 (2022).
68. S. Nimpf, H. S. Kaplan, G. C. Nordmann, T. Cushion, D. A. Keays, Long-term, high-resolution in vivo calcium imaging in pigeons. *Cell Rep. Methods* **4**, 100711 (2024).
69. T. Baden *et al.*, The functional diversity of retinal ganglion cells in the mouse. *Nature* **529**, 345–350 (2016).
70. K. Franke *et al.*, Inhibition decorrelates visual feature representations in the inner retina. *Nature* **542**, 439–444 (2017).
71. S. Weiler *et al.*, High-yield in vitro recordings from neurons functionally characterized in vivo. *Nat. Protoc.* **13**, 1275–1293 (2018).
72. D. R. Kattinig *et al.*, Chemical amplification of magnetic field effects relevant to avian magnetoreception. *Nat. Chem.* **8**, 384–391 (2016).
73. C. A. Dodson *et al.*, Fluorescence-detected magnetic field effects on radical pair reactions from femtomole volumes. *Chem. Commun.* **51**, 8023–8026 (2015).
74. C. R. Timmel, U. Till, B. Brocklehurst, K. A. McLauchlan, P. J. Hore, Effects of weak magnetic fields on free radical recombination reactions. *Mol. Phys.* **95**, 71–89 (1998).
75. G. J. Pazera, T. P. Fay, I. A. Solov'yov, P. J. Hore, L. Gerhards, Spin dynamics of radical pairs using the stochastic Schrödinger equation in MolSpin. *J. Chem. Theory Comput.* **20**, 8412–8421 (2024).
76. T. P. Fay, L. P. Lindoy, D. E. Manolopoulos, Spin relaxation in radical pairs from the stochastic Schrödinger equation. *J. Chem. Phys.* **154**, 084121 (2021).